Deformation Analysis of the Main Components in a Single Screw Compressor

2015 IOP Conf. Ser.: Mater. Sci. Eng. 90 012011

(http://iopscience.iop.org/1757-899X/90/1/012011)

Deformation Analysis of the Main Components in a Single Screw Compressor

Feilong Liu [1,3], Xueli Liao[2], Quanke Feng[1]*, Martijn Van Den Broek[3], Michel De Paepe[3]

[1] School of Energy and Power Engineering, Xi'an Jiaotong University, Xi'an, China
[2] Patent Examination Cooperation Center of the Patent Office, SIPO, Sichuan, China
[3] Ghent University, Department of Flow, Heat, and Combustion Mechanics, Gent, Belgium

qkfeng@mail.xjtu.edu.cn

*Corresponding Author

Abstract: The single screw compressor is used in many fields such as air compression, chemical industry and refrigeration. During operation, different gas pressures and temperatures applied on the components can cause different degrees of deformation, which leads to a difference between the thermally induced clearance and the designed clearance. However, limited research about clearance design is reported. In this paper, a temperature measurement instrument and a convective heat transfer model were described and used to establish the temperature of a single screw air compressor's casing, screw rotor and star wheel. 3-D models of these three main components were built. The gas force deformation, thermal-structure deformation and thermal-force coupling deformation were carried out by using a finite element simulation method. Results show that the clearance between the bottom of the groove and the top of star wheel is reduced by 0.066mm, the clearance between the side of groove and the star wheel is reduced by 0.015mm, and the clearance between the cylinder and the rotor is reduced by 0.01mm. It is suggested that these deformations should be taken into account during the design of these clearances.

Key words: single screw compressor, clearance, finite element, deformation

1. Introduction

The single screw compressor was invented by B. Zimmern based on a "pressure energy conversion device" in 1962[1]. Single screw compressors (both air and refrigeration) first appeared on the market with a rotating speed of 5000 rpm and a power of 10 HP [2]. In 1963, Peugeot managed to produce 20HP, 30HP, 40HP, and 70HP moving and stationary compressors [3]. Then, Daikin, Mitsui Seiki, Mitsubishi, Chicago Pneumatic, Hall and Grasso started to study and introduce the single screw compressor technology [4-5]. Now, the single screw compressor is widely used in many fields, including air compression, refrigeration, industrial processes, heat pumps etc.

Restricted by machining and assembly precision, certain clearances, which influence gas leakages and friction power consumption, are included in the design of the casing, screw rotor and star wheel. Oversized clearances increase the gas leakage, while clearances that are too small increase the frictional power of the lubricating oil, and can even lead to a jam of the compressor. During operation, different gas pressures and temperatures applied on the components can cause different degrees of deformation, which lead to a difference between the thermal cooperated clearance and designed clearance.

In this paper, three-dimensional models of a single screw air compressor's casing (including the cylinder), screw rotor and star wheel are described. A finite-element method was used to analyze the gas force and thermal deformation of these three main components with ANSYS. According to the obtained results, during operation, these components were subject to different deformations, which caused a different decrease of the designed clearances and could lead to a performance reduction.

2. Modeling

The models were built with Unigraphics NX and were then imported into ANSYS Workbench to perform a finite element analysis. The models of the three components (the casing, screw rotor and star wheel) were all individual models without other assembly parts and they were built on the basis of the compressor's schedule drawing.

In this paper, the casing of the air compressor was integrally cast and the model was built based on geometric relationships and measurements. The result is reproduced in Fig. 1 (a). To render the consequent calculations more efficiently, the model was first simplified as follows, also shown in Fig. 1 (b):

1) Ignore the small characteristics of the suction and exhaust end, star wheels and exhaust chamber, flanges and oil path, including most of the small lug bosses, chamfers, round corners etc. ;
2) Ignore all the bolt holes on the star wheel side, the motor side, the suction and the exhaust side;

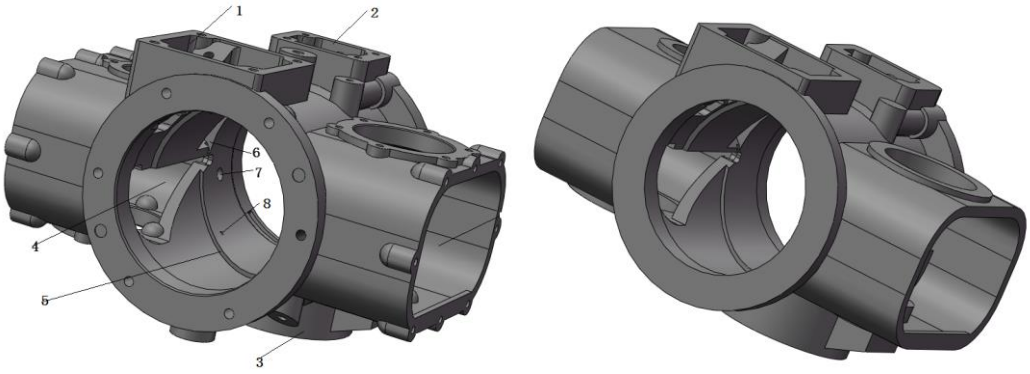

(a) Actual model (b) Simplified model

1—suction channel 2—oil path 3—exhaust channel 4—star wheel chamber 5—enclosed screw spiral 6—exhaust orifice 7—high pressure gas leak hole 8—oil injection hole

Figure 1. Actual model and simplified model of the single screw compressor.

The research presented in this paper is focused mainly on the deformation. Because the interference fit between the rotor and the axle has little influence on the deformation, the axle and the hole can be ignored. The geometries of the two star wheels are identical. The models of the rotor and star wheels built with Unigraphics NX are depicted in Fig. 2.

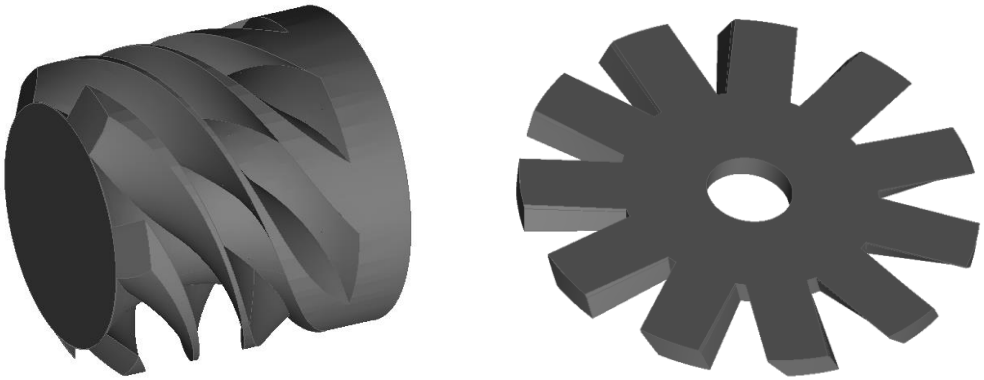

Figure 2. Unigraphics NX models of the rotor (left) and a star wheel (right).

3. Finite Element Analysis

3.1. Mesh generation

The ANSYS ICEM tetrahedral mesh (i.e. first generate the body mesh and then the surface) was used to mesh the models. In particular, a top-down mesh generation technique was used, which reduces the time to solve the geometry surface's repairing problems for some complicated geometries. Four mesh methods for a tetrahedral mesh are available in ANSYS ICEM:

1) Robust (Octree) method: a top-down mesh generation technology
2) Quick (Delaunay) method: adjust to Tetra/Mixed mesh type
3) Smooth (Advancing Front) method: adjust to Tetra/Mixed mesh type
4) TGrid method: adjust to Tetra/Mixed mesh type

Table 1. Material parameters of the single screw air compressor.

Components	Material	Poisson ratio	Elastic modulus GPa	Density kg / m^3	Linear expansion coefficient 10^{-6} / K	Thermal conductivity W/(㎡ K)
Casing	HT250	0.25	120	7300	11.8	50
Rotor and star wheel	QT600-3	0.28	170	7300	12	35.5

The Robust (Octree) method was chosen for the mesh generation. After the material's parameters (Table 1) were set, the models were meshed, shown in Figs. 3-5. Local grid refinement and "mesh smoothing" were used for some of the key parts which had small local dimensions, to improve the mesh quality. The number of grid units and nodes for the casing were 505,172 and 89,148. The rotor had 136,137 grid units and 21,137 nodes. For the star wheel, these were 31,487 and 5739 respectively. After "meshing smoothing", the mesh quality meets the requirements for the three main parts.

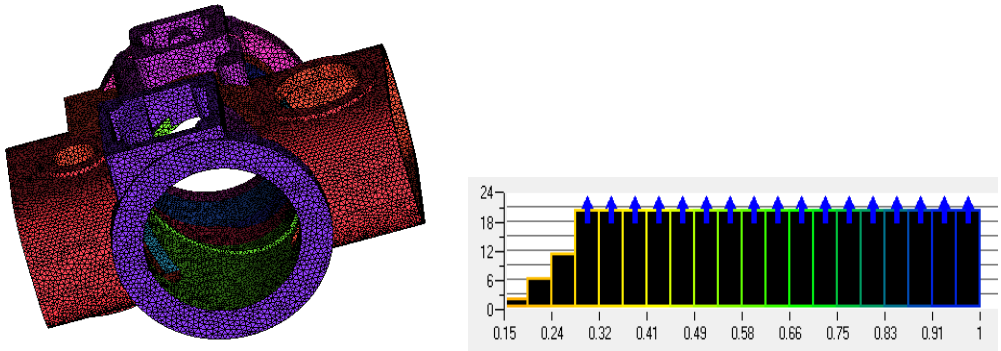

Figure 3. Mesh generation and quality of the casing.

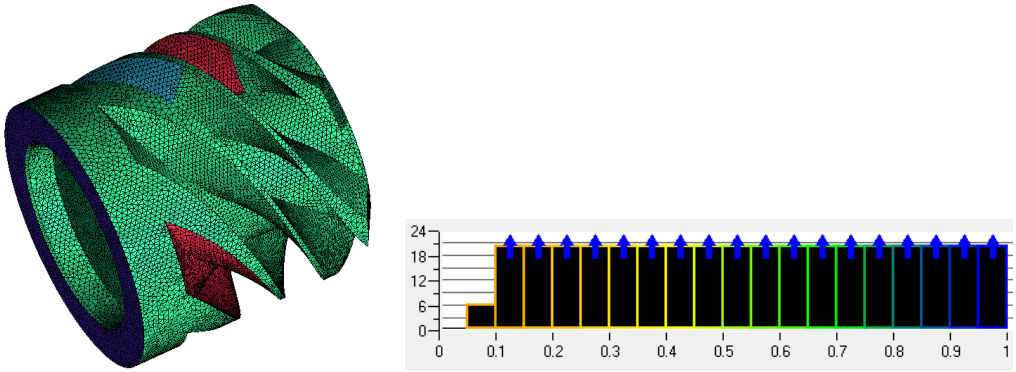

Figure 4. Mesh generation and quality of the rotor.

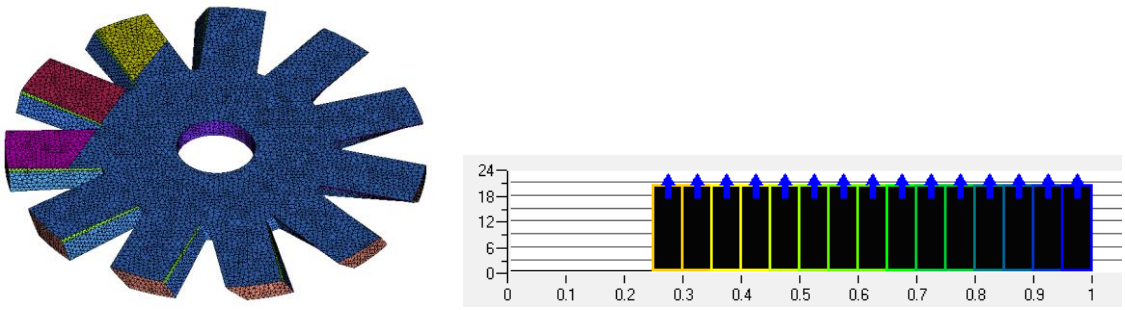

Figure 5. Mesh generation and quality of the star wheel.

3.2. ANSYS finite element analysis

The gas pressure varies during the operation of the compressor. In this paper, the time when the exhaust starts and the full-load condition (a gas flow rate of 100%) are taken as an example to perform the finite element analysis. The three continued grooves of the rotor undergo a complete compression cycle: suction-compression-exhaust. The boundary conditions imposed on the finite element model are based of the single screw compressor's operating conditions.

The pressure of the casing on the suction and exhaust ends were 0.096MPa, 0.7MPa (tested). The pressures in the three rotor grooves in the suction-exhaust direction were 0.096MPa, 0.4MPa, 0.7MPa. The pressure on the other parts out of the casing was 0.1MPa. The suction and exhaust temperature were 30℃ and 72℃.

In classical mechanics, the general dynamic equation is:

$$[M]\{\ddot{x}\}+[C]\{\dot{x}\}+[K]\{x\}=\{F(t)\} \tag{1}$$

Where [M] is the mass matrix, [C] is the damping matrix, [K] is stiffness coefficient matrix, {x} is the displacement matrix, {F(t)} is the force vector.

In Linear Static Structural Analysis, [K] should be a constant and continuous matrix, {F} should be a static force matrix which do not change with time loading on the model. Therefore, the equation is:

$$[K]\{x\}=\{F\} \tag{2}$$

This is used for calculating the structural deformation and displacement under a constant loading. The material's elastic modulus, passion ratio and linear expansion coefficient are all constant. The loading includes:

1. The external applied force or pressure.
2. Steady state inertia force, such as centrifugal force and gravity.
3. Displacement loading.
4. Temperature loading.

In this case, the pressures were used to do the Static Structural Analysis.

The three-dimensional steady-state heat conduction differential equation without inner heat source but constant property was taken as the numerical model for the temperature (t) distribution:

$$\frac{\partial^2 t}{\partial x^2}+\frac{\partial^2 t}{\partial y^2}+\frac{\partial^2 t}{\partial z^2}=0 \tag{3}$$

In a steady-state heat conduction problem, the boundary condition is the only definite condition, while the boundary conditions can be divided in three types [6]:

1) Dirichlet condition: the boundary temperature of the subject is given, t_w =constant.
2) Neumann condition: the boundary heat flux is given, q_w=constant.
3) Robin condition: $-\lambda(\frac{\partial t}{\partial n})_w=h(t_w-t_f)$,

Where t_w is the boundary temperature, t_f is the fluid's temperature and h is the heat transfer coefficient.

The surface temperature outside of the casing could be measured by a FLIR infrared thermal imager, shown in Fig. 6. The oil injection temperature was controlled around 60℃, which could certainly affect the temperature distribution in the suction chamber and the cylinder. The temperature inside the cylinder was not measured due to the oil injection (the temperature tested by the probe could be the temperature of the injection oil). The temperature of the suction and exhaust end is 56℃ and 70℃ respectively, which were enforced to the outside of the casing as the Dirichlet conditions. The temperature of the exhaust chamber was measured by the thermocouple, 72℃, which was also imposed to the inner surface of the exhaust chamber as the Dirichlet condition. The Robin condition was used for the inner surface of the casing. The convective heat transfer coefficients for the three chosen rotor grooves could be calculated, which were 360 $W \cdot m^{-2} \cdot ℃^{-1}$, 160 $W \cdot m^{-2} \cdot ℃^{-1}$, 80 $W \cdot m^{-2} \cdot ℃^{-1}$, and the related gas temperatures were 72℃, 50℃, 35℃.

Similar to the casing, the Dirichlet condition was also used for the rotor and the star wheel. According to reference [7], the temperature of the suction and exhaust end of the rotor were assumed to be 62℃ and 72℃. The temperature of the star wheel could be calculated, but details are not expatiated here. The surface and the tooth-top temperature were 64℃ and 66℃.

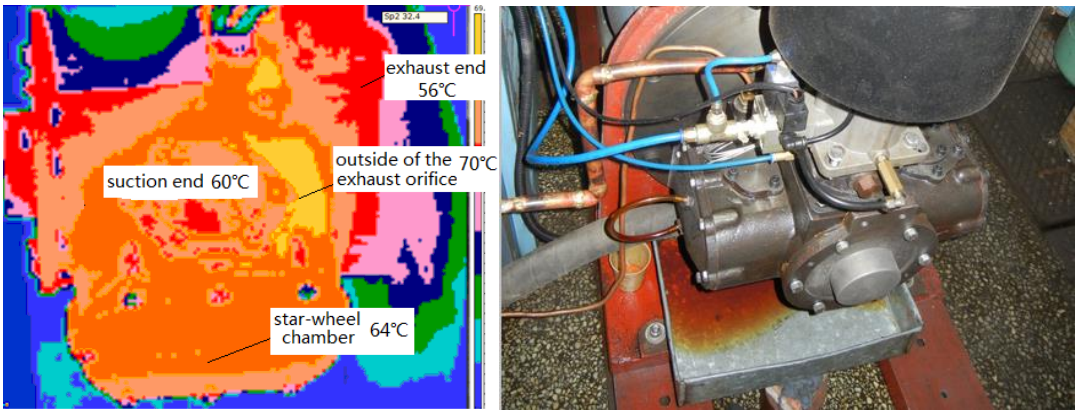

Figure 6. Temperature measurement of the casing.

First, ANSYS Workbench was used to do the static analysis and achieve the gas force deformation. Then, the temperature distribution achieved from the steady-state thermal analysis was put into the static structural analysis through the Workbench to realize the thermal-structural coupling analysis to get the thermal deformation.

Finally, the deformation caused by the combined action of the gas force and the temperature load is also acquired with ANSYS Workbench, through the built-in Thermal-Force Coupling Analysis method. The temperature distribution obtained from the Steady-State Thermal method was used as input for the Static Structural method, as well as the imposed gas pressure. The procedure is visualized in Fig. 7.

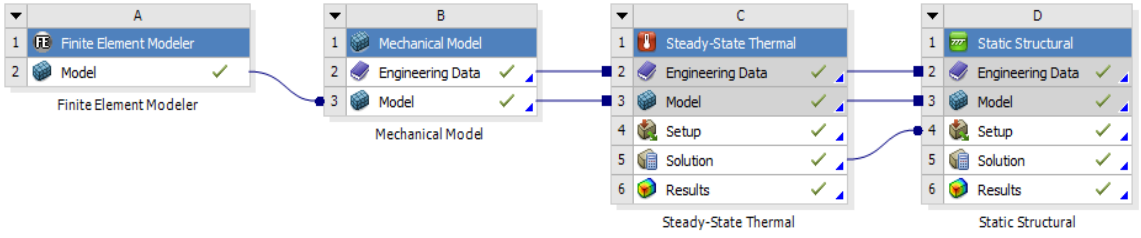

Figure 7. Procedure of the thermal-force coupling analysis.

3.3. Result and discussion

The computing results are shown in Table 2. It can be seen that the thermal deformation is much larger than that caused by the gas force, which means the gas force has little influence on the deformation. Since the actual deformation is the thermal-force coupling deformation, in the remainder of this paper we focus on this deformation.

Table 2. Deformation results.

	Gas force /mm	Thermal-structure/mm	Thermal-force/mm
Casing	9.82×10^{-3}	15.93×10^{-2}	15.98×10^{-2}
Rotor	2.49×10^{-3}	8.35×10^{-2}	8.36×10^{-2}
Star wheel	3.61×10^{-4}	4.27×10^{-2}	4.28×10^{-2}

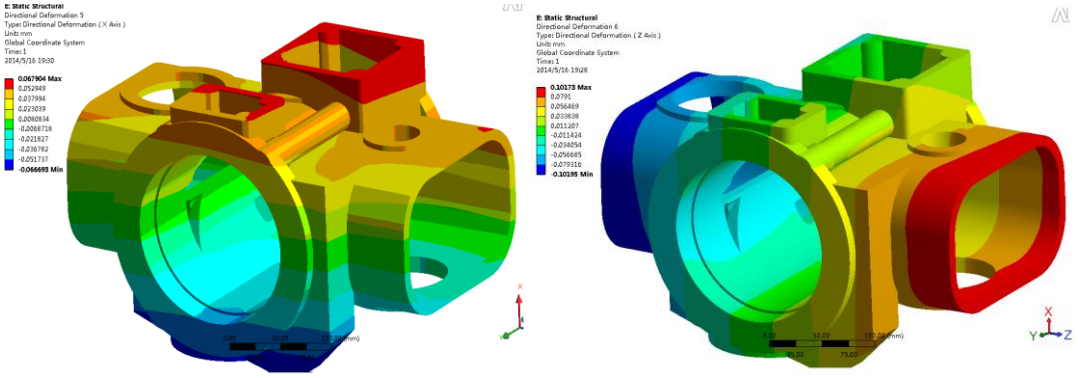

(a) Deformation in X-direction (b) Deformation in Z-direction

Figure 8. Deformation of the casing.

Fig. 8 shows the casing's deformation computing results through the direction of X and Z. In the X-direction, the maximum deformation takes place at the suction end and the minimum deformation happens at the exhaust end, which were 0.053mm and -0.067mm respectively. In the Z-direction the deformation concentrated in the star wheel chambers with a maximum deformation of 0.101mm and a minimum deformation of -0.102mm. Such large deformations could cause a change of the center distance between the star wheels and the rotor.

The deformation of the inner surface of the casing (the cylinder) is shown in Fig. 9. Obviously, the deformation increases from the suction end (minimum 0.009mm) to the exhaust end (maximum 0.047mm). The outward expanding of the cylinder may lead to a clearance change between the rotor and the cylinder.

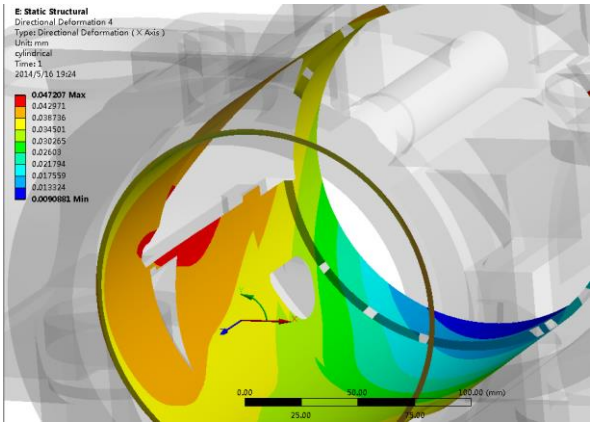

Figure 9. Deformation of the cylinder.

In order to get the accurate deformation of the cylinder in the radial direction, seven paths were delineated on the cylinder wall from the seal section to the suction end with a distance of 20mm, as shown in Fig. 10.

The computing results are given in Table 3, which shows that the largest deformation appears on the exhaust end, Path 2 and Path 3 (0.043mm).

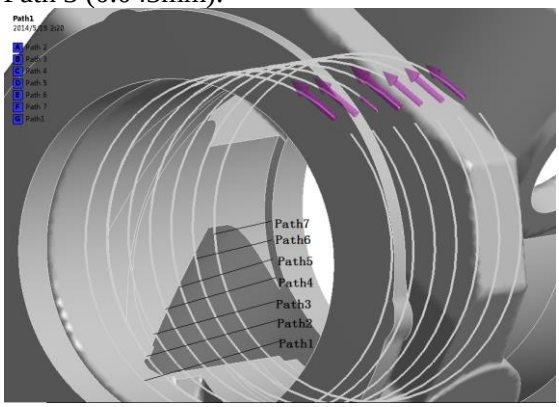

Figure 10. Paths set on the cylinder.

Table 3. Deformation of the cylinder through the radial direction.

Path	Path1	Path2	Path3	Path4	Path5	Path6	Path7
Deformation/mm	0.034	0.043	0.043	0.037	0.037	0.036	0.029

The deformation in the axial direction of the rotor was 0.082mm. Fig. 11 shows the whole deformation result in the radial (X) direction, which affects the clearance between the rotor and the cylinder. The largest deformation, which was 0.044mm, took place at the rotor's sealing edge, and the smallest deformation (0.021mm) was on the bottom of the middle groove.

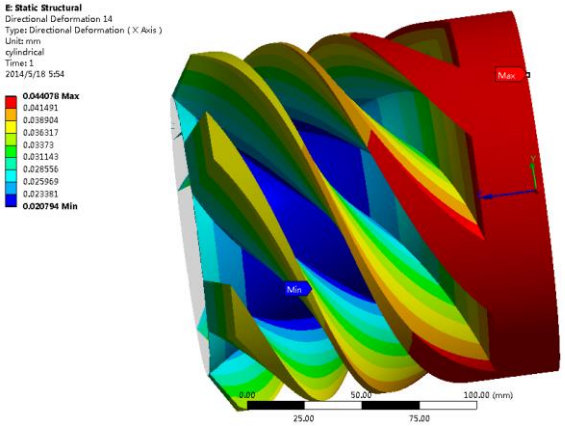

Figure 11. Deformation of the rotor in the radial direction.

Similar to the cylinder, for the radial direction, seven paths, with locations corresponding to those on the cylinder, were also set to get the accurate deformation, as depicted in Fig. 12. The result is shown in Table 4. The maximum deformation also happens at the exhaust end and decreases towards the suction end, from 0.044mm to 0.036mm.

Table 4. Deformation of the 7 paths on the rotor.

Path	Path1	Path2	Path3	Path4	Path5	Path6	Path7
Deformation/mm	0.044	0.043	0.043	0.041	0.040	0.038	0.036

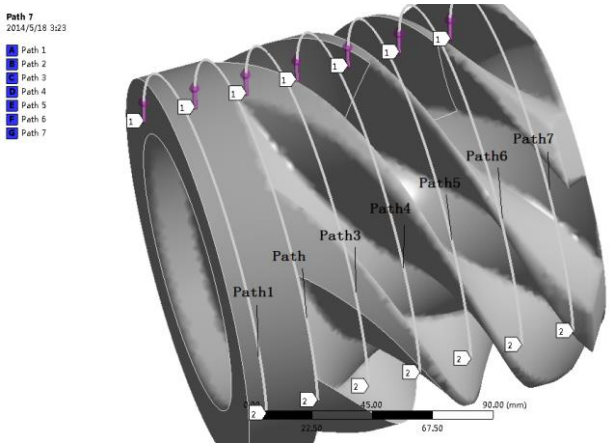

Figure 12. Path set of the rotor.

To research the clearance between the rotor groove and a star wheel tooth, the deformation on the bottom and both sides of the rotor groove in the normal direction also needs to be taken into account. Due to the rotor's complicated geometrical shape, it is hard to get the result directly from the calculation mentioned above. Since the groove bottom's projection is circular, a path is set as in Fig. 13 (a). Then the deformation in the path's normal direction coincides with the deformation of the groove's bottom. Similarly, the path for both sides of the groove can be set as in Fig. 13 (b). Thus, the required deformation corresponds to the deformation in the path's normal direction. The maximum of the bottom was 0.024mm (exhaust end) and the minimum was 0.021mm (suction end). For the groove sides, they were the same everywhere, 0.009mm.

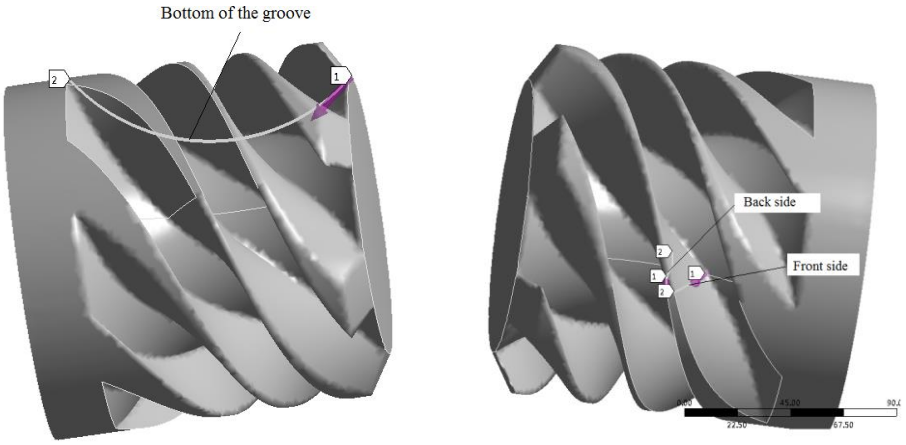

（a）Path set for the bottom of the groove （b）Path set for the two sides of the groove

Figure 13. Paths set on the groove's bottom and flanks.

The computing result of the star wheel is shown in Fig. 14. The star wheel extends from the central hole to the top of the teeth. The central deformation is 0.007mm, while on the top of a tooth the deformation is maximum, 0.042mm. Similarly to the rotor, paths were set to acquire information on the deformation of the tooth's edges, as shown in Fig. 15. The tangential deformation on the top of a tooth is 0.042mm, and it is 0.006mm for each side.

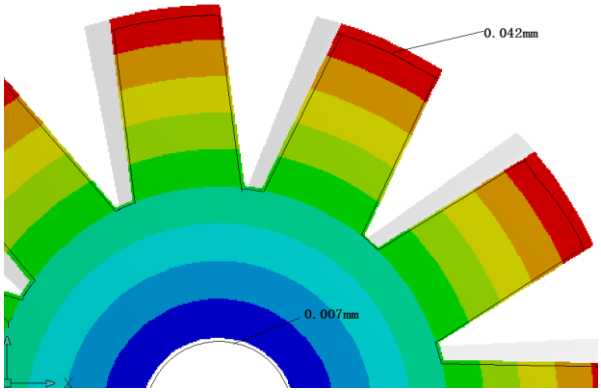

Figure 14. Deformation of the star wheel.

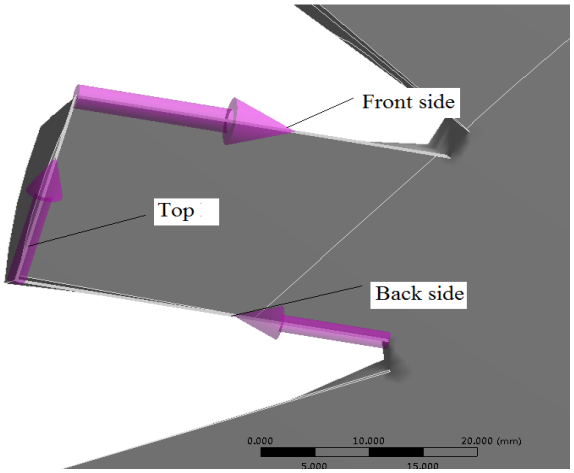

Figure 15. Paths set of a star wheel tooth.

The designed clearances of the compressor investigated (type of 9 $m^3 \cdot min^{-1}$) in this paper are given in Table 5, as well as some other types of compressors' designed clearances applying on the market. According to the computing result, during the operation, these clearances change due to the thermal-force coupling deformation.

Table 5. Designed clearances of the air compressors.

Components	Clearance/mm (different types of compressors)		
Types	9 $m^3 \cdot min^{-1}$	3 $m^3 \cdot min^{-1}$	12 $m^3 \cdot min^{-1}$
Cylinder and rotor	0.02	0.02	0.03
Top of the tooth and bottom of the groove	0.04—0.07	0.03—0.05	0.06—0.08
Flank of the tooth and the groove	0.03—0.05	0.02—0.04	0.05—0.07

For the rotor and the cylinder, they have the same deformation direction, but the rotor experiences a larger deformation than the cylinder, so the clearance decreases. Table 6 shows the deformation difference between the cylinder and the rotor for the seven paths. The largest change takes place at the rotor's sealing edge (0.10mm).

Table 6. Clearance change.

Path	Path1	Path2	Path3	Path4	Path5	Path6	Path7
Cylinder /mm	0.034	0.043	0.043	0.037	0.037	0.036	0.029
Rotor /mm	0.044	0.043	0.043	0.041	0.040	0.038	0.036
Difference/mm	0.01	0.000	0.000	0.004	0.003	0.002	0.007

The tooth top of the star wheel expands with 0.042mm, while the bottom of the rotor groove has a maximum deformation of 0.024mm, which is in the opposite direction of the tooth top. Thus, their clearance reduces by 0.066mm, close to the designed clearance, which would cause an elastic contact and lead to the wear of the star wheel.

Similarly, because of the opposite deformation direction, the clearance between the side of the rotor's groove and the side of the star wheel's tooth also reduced by 0.015mm, which was within the designed clearance.

4. CONCLUSIONS

1) A symmetric deformation could certainly happen to the casing and could lead to a change of the center distance between the star wheel and the rotor due to the thermal and gas force factors.

2) The largest deformation of the cylinder appears in the exhaust end, while that of the rotor happens in the rotor's sealing edge. Besides, the largest clearance change between the rotor and cylinder also takes place here, with a decrease of 0.10mm.

3) The decrease of the clearance between the top of the star wheel's tooth and the bottom of the rotor's groove is close to the designed clearance. As a result, a hard contact may turn up and finally lead to wear of the star wheel.

4) The clearance between the plank of a star wheel's tooth and the rotor's groove also reduces by 0.015mm, which is allowed by the designed clearance of 0.03mm-0.05mm.

5) It is suggested to do the thermal-force coupling deformation analysis for these three main parts of the air compressor, which could serve as a guide for the determination of the designed clearances.

References

[1] Zimmern B. Worm rotary compressors with liquid joints. U.S. Patent No. 3133695; 1965.
[2] Zimmern B. From Water to Refrigerant: Twenty Years to Develop the Oil Injection-free Single Screw Compressor [C]. Purdue, 1984: 513-518.
[3] Zimmern B, Patel GC. Design and Operating Characters of the Zimmern Single Screw Compressors[C]. Purdue, 1972: 96-99.
[4] Deren Wang, Development Situation of the Single Screw Compressor [J]. Electromechanical Device, 1994, (1): 2-6.
[5] Company C P T .A Revolution in Air Compressor Technology [J]. Transactions of the ASME, Journal of Applied Mechanics,1987: 217-224.
[6] J.H.Wu, G.X. Jing. Investigation on Suction Process of Oil-Flooded Rotary Positive Displacement Compressors [J]. Fluid Machinery, 1995, (5): 7-10.
[7] Chukanova E, Stosic N, Kovacevic A. Investigation of Start Up Process in Oil Flooded Twin Screw Compressors [C]. Purdue, 2012, 1138.